water

MDPI

Article

Integrating Rainfall Distribution Patterns and Slope Stability Analysis in Determining Rainfall Thresholds for Landslide Occurrences: A Case Study

Meen-Wah Gui [1,*], Hsin-An Chu [1], Ming-Chien Chung [2] and Lan-Sheng Chih [3]

[1] Department of Civil Engineering, National Taipei University of Technology (Taipei Tech), Taipei 106344, Taiwan; ge-10524@gov.taipei
[2] Arbel Technical Consultants, Inc., Taipei 234620, Taiwan; yuyenpe@gmail.com
[3] Geotechnical Engineering Office, Public Works Department, Taipei City Government, Taipei 110210, Taiwan; ge-10913@gov.taipei
* Correspondence: mwgui@ntut.edu.tw

Abstract: After a series of rainfall-related slope incidents that threatened immediately protected entities, the Taipei City government initiated a slope deformation monitoring and investigation program for potential landslides in its administrative districts and a review of its current rainfall thresholds for landslide occurrences, which is the aim of this study, in 2021 for better preparedness in facing the extreme weather- and climate-related natural hazards. Due to the limited availability of historical data, this study employed a physically based method to derive rainfall thresholds for landslide occurrences by integrating different rainfall distribution patterns into infiltration and slope stability analyses. The study examined four rainfall patterns—uniform, intermediate, advanced, and delayed—to assess their impact on slope failure mechanisms. Results indicate that advanced rainfall patterns (where peak rainfall occurs early) trigger the fastest failures, while delayed rainfall patterns lead to gradual groundwater accumulation, causing slope destabilization over longer durations. The study also found that short-duration rainfall (24 h) mainly triggers shallow landslides, whereas prolonged rainfall (72 h) leads to deep landslides. The study's findings are crucial for early landslide warning systems, which provide different mitigation strategies based on the expected rainfall duration and provide a scientific basis for authorities to revise and integrate new rainfall thresholds into their real-time landslide warning systems.

Keywords: rainfall thresholds; rainfall patterns; early landslide warning system; alert and action warnings; slope stability; numerical analysis

check for updates

Academic Editors: Qihang Li, Xiaoshuang Li and Jiang Song

Received: 17 March 2025
Revised: 15 April 2025
Accepted: 16 April 2025
Published: 21 April 2025

Citation: Gui, M.-W.; Chu, H.-A.; Chung, M.-C.; Chih, L.-S. Integrating Rainfall Distribution Patterns and Slope Stability Analysis in Determining Rainfall Thresholds for Landslide Occurrences: A Case Study. *Water* **2025**, *17*, 1240. https://doi.org/10.3390/w17081240

Copyright: © 2025 by the authors. Licensee MDPI, Basel, Switzerland. This article is an open access article distributed under the terms and conditions of the Creative Commons Attribution (CC BY) license (https://creativecommons.org/licenses/by/4.0/).

1. Introduction

Rainfall-induced landslides threaten human lives and the natural environment, especially in mountainous regions. For example, in early August 2015, Typhoon Soudelor, which triggered massive landslides in northern Taiwan, caused at least 8 people to die, while 420 others sustained injury and approximately 100 people went missing in the Wulai District during the storm on August 8 [1]. Fushan rainfall station, located upstream of Wulai, recorded a cumulative rainfall of 253 mm within 3 h in a recurrence period of 100 to 200 years and a cumulative rainfall of 768 mm over 24 h in a recurrence period of more than 200 years. This event highlighted the need for accurate prediction of the relationship between the amount of rainfall and the initiation of landslides. The risk associated with landslide events is expected to rise due to projected extreme climate conditions, making accurate prediction crucial for effective risk reduction [2]. Rainfall thresholds, representing

the amount of rainfall likely to initiate landslides, are crucial in landslide prediction for early warning systems to issue timely alerts. Since landslides are rare and probabilistic events, it is necessary to derive different threshold curves for different landslide probability conditions to enhance the reliability and accuracy of landslide warnings [3].

Segoni et al. [4] presented a comprehensive review of advancements in the use of rainfall thresholds for landslide forecasting between 2008 and 2016. They analyzed 107 peer-reviewed studies, categorizing 115 thresholds based on publication details, geographic scope, dataset features, and threshold definition methods and pointed out some positive shifts in recent studies, such as a move toward more consistent and transparent ways of defining rainfall thresholds, better record keeping with respect to landslides and rainfall, and a growing use of probability-based thresholds to improve early warning systems.

Many studies have derived rainfall thresholds by statistically analyzing historical rainfall and landslide data (e.g., He et al. [5], Abraham et al. [6,7], Jordanova et al. [8], and Roccati et al. [9]). First, He et al. [5] employed a large landslide inventory covering events between 1998 and 2017, quantile regression approaches, and a statistical modeling technique to derive a rainfall threshold for predicting landslide occurrence nationally in China. They defined a rainfall event continuous rainfall separated by a no-rainfall period of at least 24 h and established two kinds of rainfall thresholds—accumulated rainfall-duration thresholds and thresholds normalized by mean annual precipitation, based on the merged rainfall product and the Climate Prediction Center morphing technique rainfall product, respectively. They found that the thresholds vary for rainy and non-rainy seasons and short versus long durations, and their rainfall event-duration threshold is lower than that found in previous studies. Abraham et al. [6] explored the relationship between rainfall and landslide occurrence in Wayanad, India, a region prone to landslides due to heavy monsoons, using data on daily rainfall and landslide events between 2010 and 2018. They found a rain gauge selected based on the most extreme rainfall performed better than the nearest gauge. They used the statistical frequentist method to derive the power-law-based rainfall intensity–duration thresholds for use in regional-scale early landslide warning systems. However, for the prediction of rainfall-induced landslides in Kalimpong, India, Abraham et al. [7] adopted the SIGMA (sistema integrato gestione monitoraggio alerts—an integrated system for management, monitoring, and alerting) model initially developed in Italy. The model used historical cumulative rainfall and landslide data between 2010 and 2015 to derive rainfall thresholds and defined four alert levels: “red”, “orange”, “yellow”, and “green”. The validation of the SIGMA model correctly predicted slow movement events, with only two missed alarms. However, the model produced a relatively high count of false alarms.

Finally, to provide early warning systems in Slovenia with a more accurate rainfall threshold for shallow landslides, Jordanova et al. [8] used an automatic tool (CTRL-T) to analyze historical rainfall and landslide data and used the statistical frequentist approach to derive reliable power-law-based thresholds that connect the accumulated-event rainfall with the duration of the rainfall event. They found that areas with higher average rainfall can withstand more precipitation before landslides and that sedimentary rocks are more prone to landslides than magmatic and metamorphic rocks. Likewise, Roccati et al. [9], who investigated the relationship between rainfall and shallow landslide initiation in the Portofino promontory, a Mediterranean area prone to landslides, also used the frequentist approach to analyze the long-term rainfall trends in the region using historical landslide and rainfall data between 1910 and 2019 and derived the intensity–duration threshold. They used the statistical Mann–Kendall test and the Theil–Sen non-parametric regression technique to detect increasing trends in short-duration precipitation and rainfall rates. They also proposed that a potential increase in future landslide risk is likely to be due to more

frequent threshold exceedance. However, empirically derived thresholds may be ineffective for landslide prediction over large areas [2].

Some studies (e.g., Abraham et al. [10], Dikshit et al. [11], and Deng et al. [12]) have used probabilistic approaches to derive the rainfall threshold. Firstly, using the rainfall and landslide data between 2010 and 2018, Abraham et al. [10] derived a regional-scale rainfall intensity–duration threshold for landslide occurrence in the Idukki district of India. They found the significance of antecedent rainfall on landslide events; as the number of days before landslide events increases, the distribution of events shifts toward antecedent rainfall conditions, with bias increasing from 72.12% to 99.56% as the temporal window expands from 3 to 40 days. Dikshit et al. [11] assessed the rainfall threshold and landslide susceptibility for the Samdrup Jongkhar–Trashigang highway region in eastern Bhutan using the Poisson probability model and the analytic hierarchy process (AHP), respectively. They derived the rainfall thresholds using 30-day antecedent rainfall data and landslide events occurring between 2014 and 2017 to identify areas prone to landslides along the highway. Deng et al. [12] employed landslide events occurring between 2010 and 2020 and probability quantile regression methods to investigate rainfall thresholds for shallow landslides in areas with different lithological units in Guangzhou, China. They used accumulated event rainfall and rainfall event duration data to derive rainfall thresholds. They found that intrusive rock units are particularly susceptible to landslides and that continuous rainfall lasting for 1 to 10 days significantly affects shallow landslides in Guangzhou.

In recent advancements, Distefano et al. [13] applied artificial neural networks to refine landslide prediction using precipitation and soil moisture data. They used data from two case studies in Sicily (Italy) and the Bergen area (Norway) to test the approach across varying climatic and geomorphological conditions. Their artificial neural network system adopted different combinations of precipitation duration, intensity, cumulative amount, and soil moisture at different depths to determine landslide-triggering rainfall thresholds. They concluded that landslide-triggering systems using soil moisture and precipitation data outperform those using precipitation data only.

Guo et al. [14] integrated hydrological models with slope stability analysis to provide a mechanistic understanding of rainfall infiltration. They analyzed rainfall thresholds for shallow landslides in the Rasuwa district of Nepal, an area highly susceptible to landslides, especially after the 2015 earthquake. The study used a physically based model, combining a dynamic hydrological model with an infinite slope stability model to simulate landslide stability conditions based on rainfall data and terrain characteristics for effective landslide risk reduction in a data-scarce environment. They found that a 15-day intensity-antecedent rainfall threshold performed best; the approach provided a crucial step towards developing a landslide threshold for vulnerable, data-scarce, and landslide-prone areas. Insufficient hydrological and geotechnical parameters on a large scale may hamper the use of deterministic methods [3].

Researchers such as Bordoni et al. [15], Ligong et al. [16], and Gonzalez et al. [17]) have applied hybrid methods and conducted reviews of methods and publications concerning rainfall thresholds. For example, Bordoni et al. [15] employed empirical and physically based methods to derive rainfall thresholds for shallow landslides in the northern Italian Apennines. The empirical thresholds used statistical analysis of rainfall and landslide events between 2000 and 2018, while the physically based models integrated slope hydrology and stability analyses using data from a test site, which was significantly prone to shallow landsliding. The study concluded that the physically based thresholds showed better reliability than empirical thresholds in predicting slope failures because they take into account the antecedent soil hydrological conditions. Meanwhile, in Malaysia, Ligong

et al. [16] presented an update for the development and application of rainfall thresholds for sediment-related disasters. Conventionally, researchers in Malaysia determine rainfall thresholds using empirical models. The study examine data collection, threshold identification, and validation of models to improve landslide and mudflow management. They concluded that the validation process is the key to successfully applying rainfall threshold in Malaysia. Finally, after conducting a systematic review of publications from 2008 to 2021 on rainfall thresholds for the prediction of landslide occurrence, Gonzalez et al. [17] found that 69.3% of the studies involved only statistical methods, with intensity–duration and cumulative rainfall identified as key parameters to define rainfall thresholds; typical limitations such as short data collection periods and failure to register the time of landslide occurrence compromise the relationship between rainfall data and the occurrence of landslides. Relations concerning geological–geotechnical conditions, the time scales of rainfall data, rain-gauge density for categorization of thresholds, and the criteria used to define the cumulative rainfall period have also attracted limited attention.

In summary, deriving rainfall thresholds for landslide occurrences is critical to landslide hazard assessment and early warning systems. Three commonly employed approaches, i.e., empirical–statistical approaches, physically based (hydro-mechanical) models, and probabilistic approaches, may be used to derive thresholds based on their methodological frameworks, as well as their applications in geomorphology and engineering geology. Hybrid approaches may also be employed, which may combine either two of the above three methods or AI-based machine learning approaches [13,18].

With 55% of its land covered by slopes [19], Taipei City has seen an increase in landslides due to extreme rainfall events. The lack of localized or regional-scale rainfall thresholds for landslide occurrences has resulted in Taipei City relying solely on a few generalized thresholds, often leading to inaccurate warnings (false positives) and severe damage. Thus, deriving accurate and site-specific rainfall thresholds is important to protect the lives of city residents and their properties. In 2012, Typhoon Saola caused several slope failures in Nangang District, Taipei, displacing retaining walls and damaging infrastructure. Several rainfall-related slope issues in the following years have prompted the Taipei City government to initiate a slope deformation monitoring and investigation program for potential landslides in its administrative districts and to review its current rainfall thresholds for the prediction of landslide occurrences, which is the aim of this study, in 2021 in order to improve preparedness for extreme weather- and climate-related natural hazards. Due to the limited availability of historical landslide data, determining rainfall threshold using the empirical–statistical method would be ineffective and unreliable. Thus, this study adopted a combined geotechnical and physically based method to derive site-specific thresholds for landslide occurrences. The main methods employed in this study involve a series of boreholes, slope monitoring, and numerical analyses that integrate different rainfall distribution patterns into infiltration and slope stability analyses.

2. Background of the Study Slope

2.1. Site Topography

The study slope is situated in Nangang District, Taipei City—specifically, the slope below the Baoshutang Tea Garden, bounded by coordinates of *N* 2,768,800 m to *N* 2,768,900 m and *E* 316,600 m to *E* 316,700 m [20] (Figure 1). Google Earth satellite image revealed that the topography of the study site in December 2006 (Figure 2a) already had frame beams installed to stabilize the left-hand side of the study site. The study site shows a trend of a high elevation in the northeast to a low elevation in the southwest. The lithology of the Miocene Daliao Formation, primarily composed of shale and sandstone, makes up the site.

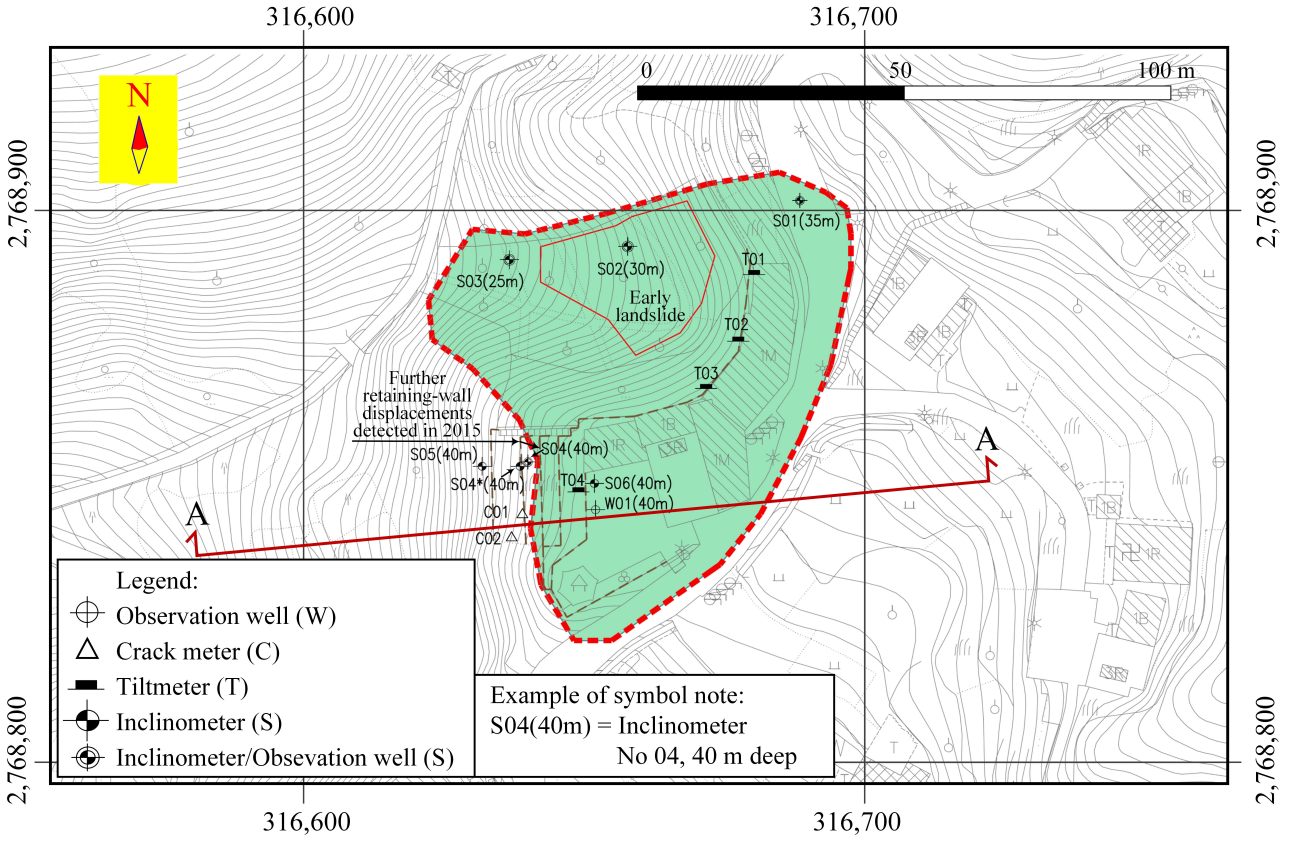


Figure 1. Layout showing the locations of boreholes and monitoring devices at the study site.

During Typhoon Sinlaku in 2008, the site experienced a shallow landslide to the left of the stabilized slope (Figure 2b), prompting the authorities to undertake further remedial measures, such as the installation of frame beams for slope protection and longitudinal drainage ditches across the whole slope. The topography remained unchanged throughout 2010 (Figure 2c), but in July 2011 (Figure 2d), a substantial area of the surface of the opposite slope was exposed, indicating a shallow slope failure had occurred between December 2010 and July 2011. In 2012, Typhoon Saola displaced the retaining walls of the platform west of the residential building (Figure 2e). Subsequently, Typhoon Soudelor (August 2015) and Typhoon Dujuan (September 2015) caused further displacement of the retaining walls of this platform, breaking the drainage ditch behind the wall. The vegetation on the slope has been growing lushly since October 2016 (Figure 2f–h), primarily due to the absence of typhoons during this period. For improved preparedness in light of extreme climate change, the Taipei City government initiated a program to monitor the deformation of slopes in Taipei City and to formulate a specific disaster response plan, which includes site-specific rainfall thresholds for the prediction of landslide occurrence for the benefit of the protected entities on this slope. The disaster response plan designates residents and property as protected entities.

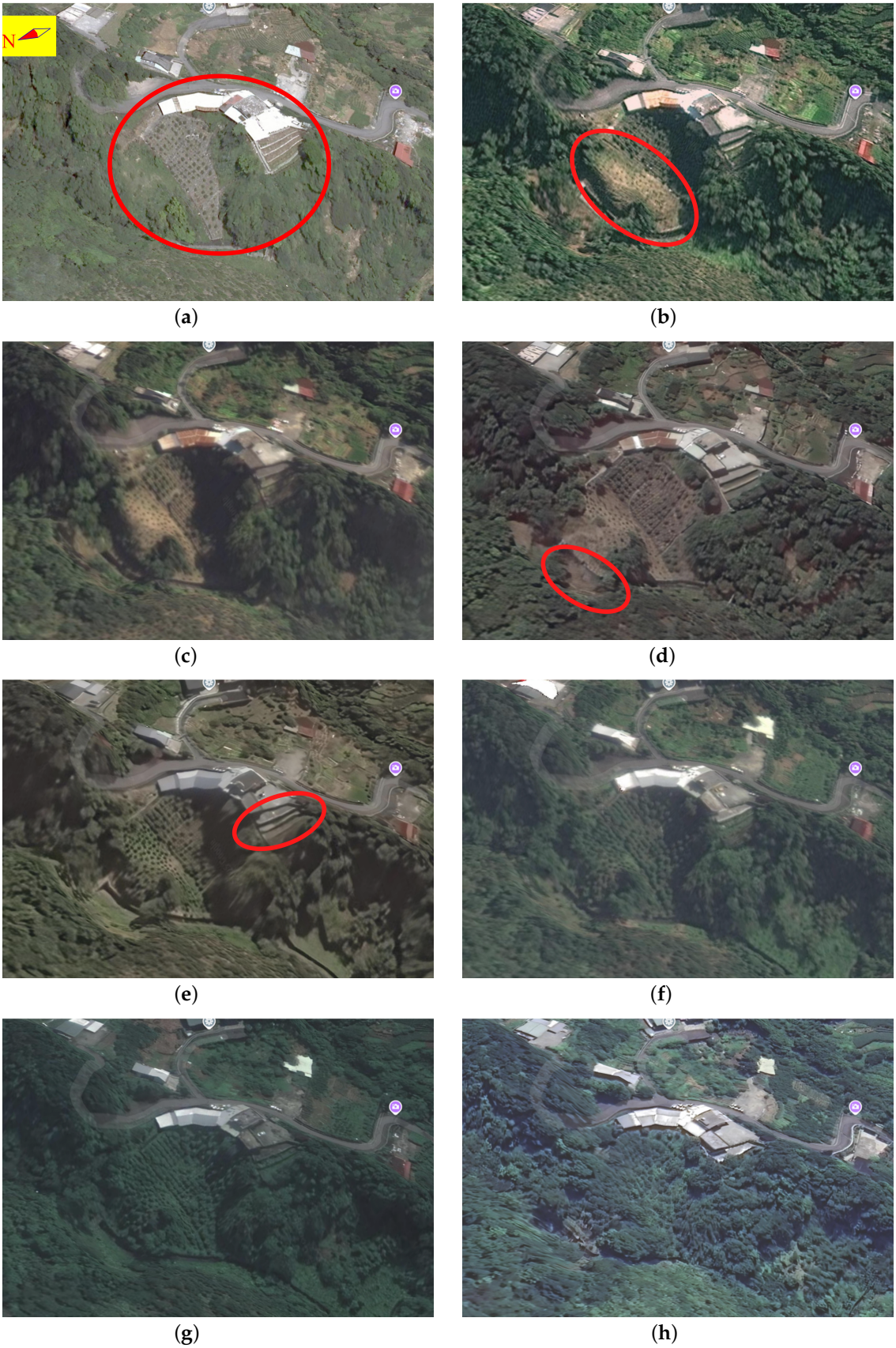


Figure 2. Google Earth satellite images showing the evolution of the study slope from Dec 2006 to Jul 2023: (**a**) Dec 2006: study site featuring frame beams; (**b**) Jan 2010; shallow landslide detected on site; (**c**) Dec 2010: unchanged terrain; (**d**) Jul 2011: exposed slope face revealed; (**e**) Jan 2014: retaining-wall displacements; (**f**) Oct 2016: lush vegetation growth; (**g**) Oct 2017: lush vegetation growth; (**h**) Jul 2023: lush vegetation growth (Google Earth Pro [21]).

2.2. Rainfall Distribution Patterns

Typhoons are responsible for 47.5% of the annual rainfall on the island of Taiwan [22]. By considering the temporal, intensity, and distribution characteristics of rainfall and the role and circulation patterns of typhoons in causing rainfall, Huang [23] categorized typhoon-related rainfalls on the island into four distribution categories. According to Huang [23], the first category is associated with a prolonged retention period and is more destructive because of its heavy and prolonged rainfall. The second category is often associated with two heavy rainfalls, where an approaching typhoon causes the first rainfall, while the second, which is usually more intense than the first rainfall, is due to peripheral circulation after the typhoon has left. The third category also has two rainfall events, but the first rainfall is more intense than the second, and there is a longer interval between the two rainfalls. In contrast, the fourth category is associated with single-peak distribution, which usually occurs after a typhoon has left behind strong wind and rainfall [23].

Figure 3 shows how this study defines a rainfall event. An effective rainfall begins when the hourly rainfall exceeds 4 mm and ends when the hourly rainfall remains below 4 mm for a continuous period of three hours [24]. The interval between the start and end of an effective rainfall is defined as a continuous rainfall event. In contrast, the time from the start to the end of a rainfall event, including short periods without rain during the event, is defined as rainfall duration (in hours) [24].

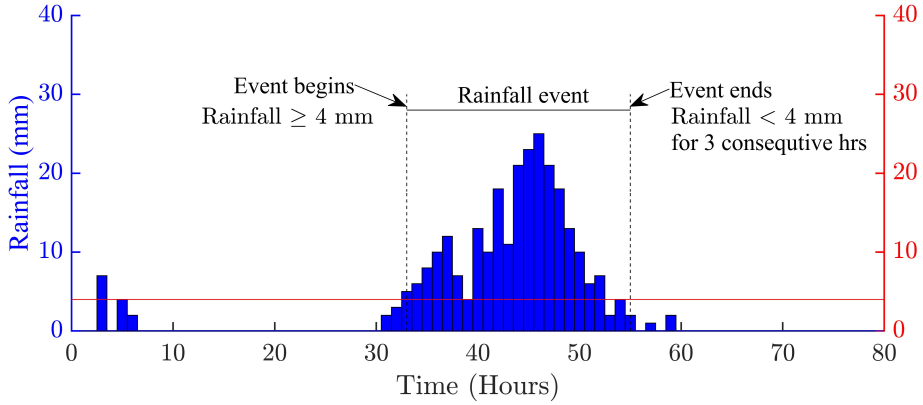


Figure 3. Definition of a rainfall event.

The fourth category, i.e., the single-peak distribution pattern, can be further sub-categorized into four rainfall distribution patterns—uniform, intermediate, advanced, and delayed (Figure 4, [25–27])—each of which strongly impacts the local climate, ecosystems, and water management practices. These patterns have the same amount of rainfall, but their maximum intensity occurs at different times [27]. A uniform pattern is where the rainfall is evenly distributed over time (Figure 4a). An intermediate or middle-peak distribution is when the distribution resembles a bell or Gaussian curve in which the rainfall is concentrated around the middle of the rainfall duration (Figure 4b). An advanced pattern is where the peak rainfall occurs earlier in the time frame under analysis; in other words, it shows a skewed distribution where the rainfall intensity declines sharply after the initial peak, leading to less rainfall intensity towards the latter part of the end of the duration (Figure 4c). A delayed pattern is the opposite of an advanced pattern, characterized by a significant peak in the latter part of the rainfall duration (Figure 4d). The rainfall pattern significantly impacts the type and time of failure in slope warning assessments. Theoretically, a uniform rainfall pattern may lead to shallow slope failures due to the consistent accumulation of water near the surface; a delayed rainfall pattern might cause groundwater to rise slowly, leading to delayed and triggered deep failure, while an advanced pattern might induce rapid infiltration and immediate instability [28,29].

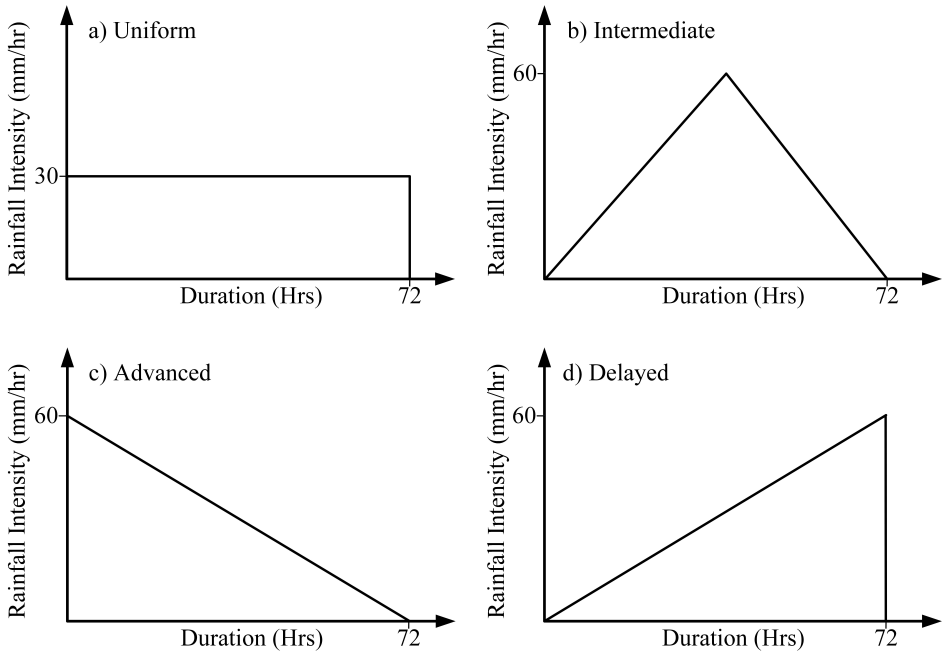


Figure 4. The four temporal rainfall patterns used in this study. All patterns produce the same amount of rainfall.

Between 2003 and 2021, the island recorded 38 typhoon-related heavy rainfalls; of the 38 rainfalls, 5 were associated with the first category, 6 with the second category, another 6 with the third category, and 21 with the fourth category. Further classifying the fourth single-peak category into sub-rainfall distribution pattern,1 falls into the advanced pattern, 16 into the intermediate pattern, 3 into the delayed pattern, and 1 into the uniform pattern. Thus, the intermediate rainfall pattern is not only the most prevalent but also the most predominant rainfall pattern.

2.3. Site Geology

To collect data for detailed study, a ground investigation via a series of boreholes was conducted to establish the soil and rock profiles, as well as the material parameters, for the numerical analysis. A monitoring system, which included crack meters, tiltmeters, inclinometers, and an observation well, was set up on the study site. The instrumentation locations are shown in Figure 1. The geological cross-section (A–A) derived from the information of the borehole logs of borehole Nos. S01, S02, S04, and S05 from the site investigation, in which boreholes S01, S04, and S05 were drilled to a depth of 40 m, is shown in Figure 5. It was discovered that the site was covered by a layer of fill between depths of 0 and 2.15 m, a weathered sandstone–shale (SS/SH) inter-layer between 2.15 m and 21.25 m, and a fresh sandstone–shale (SS/SH) inter-layer between 21.25 m and 40 m.

Between 2021 and 2023, four typhoons brought heavy rains to the island of Taiwan: Typhoon Chanthu (7 September 2021), Typhoon Kompasu (10 October 2021), Typhoon Nesat (10 October 2022), and Typhoon Mawar (29 May 2023). Among these events, Typhoon Kompasu and Typhoon Nesat, together with the 24 May 2022 Plum Rain, brought rainfall exceeding 300 mm. Figure 6 shows the historical rainfall intensity and the corresponding groundwater levels versus elapsed time records before and after these three rain events. Elapsed time is adopted because rainfall duration explicitly measures the time from the start to the end of a continuous or intermittent rainfall event. In contrast, the elapsed time considers the time frame from any moment until a specific time, including dry periods. The groundwater level during Typhoon Kompasu (Figure 6a) and the 24 May 2022 Plum Rain (Figure 6b) was measured via the dual-function inclinometer/observation well (S04)

while that during Typhoon Nesat (Figure 6c) was taken as the reading from observation well W01 because S04 was found to be damaged during Typhoon Nesat. The locations of S04 and W01 are shown in Figures 1 and 5, respectively. S04 is located on the vegetated sloping terrain near the crest of the slope, while W01 is located on the crest of the slope with a paved surface.

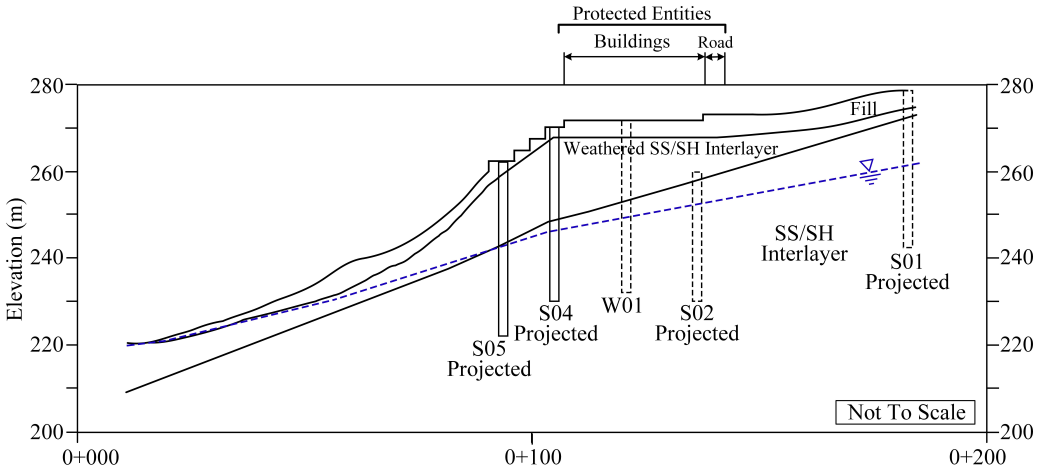


Figure 5. Geological cross section (A–A) of the study slope.

In all three plots, groundwater levels rise in response to rainfall, but the magnitude and timing of the response vary with well location and surface conditions. In addition, all responses show a lag effect, in which the groundwater level increases after sustained or intense rainfall, although not instantly. The groundwater level in Figure 6a,b shows a more sensitive response to rainfall; the groundwater levels rise more sharply and earlier after rainfall begins than in Figure 6c. The reason is likely due to faster down-slope lateral water movement down-or higher infiltration rates on the sloping terrain. The groundwater level in Figure 6a,b also tend to decline faster after rainfall ends, suggesting better drainage or runoff pathways on the vegetated terrain. In contrast, Figure 6c shows a more gradual and buffered response, where the groundwater level increases more slowly, even during intense rainfall. This scenario is likely due to the low level of rainfall infiltration through the impervious paved surface. Moderate groundwater recharge in W01 is primarily caused by delayed vertical seepage or subsurface lateral inflow from up-slope or adjacent areas. Table 1 quantitatively compares the regular day and peak groundwater levels recorded in S04 and W01 within these 180 days; the result indicates that these rainfall events caused the groundwater level of the study slope to rise by at least 2.09 m.

Table 1. Peak groundwater levels recorded during the three rain events.

Rain Event	Observation Well No.	Before Rain (m)	After Rain (m)	Rise in Water Level (m)
Typhoon Kompasu	S04	−16.10	−13.66	2.44
May 24 Plum rain	S04	−16.36	−13.10	3.26
Typhoon Nesat	W01	−13.64	−11.55	2.09

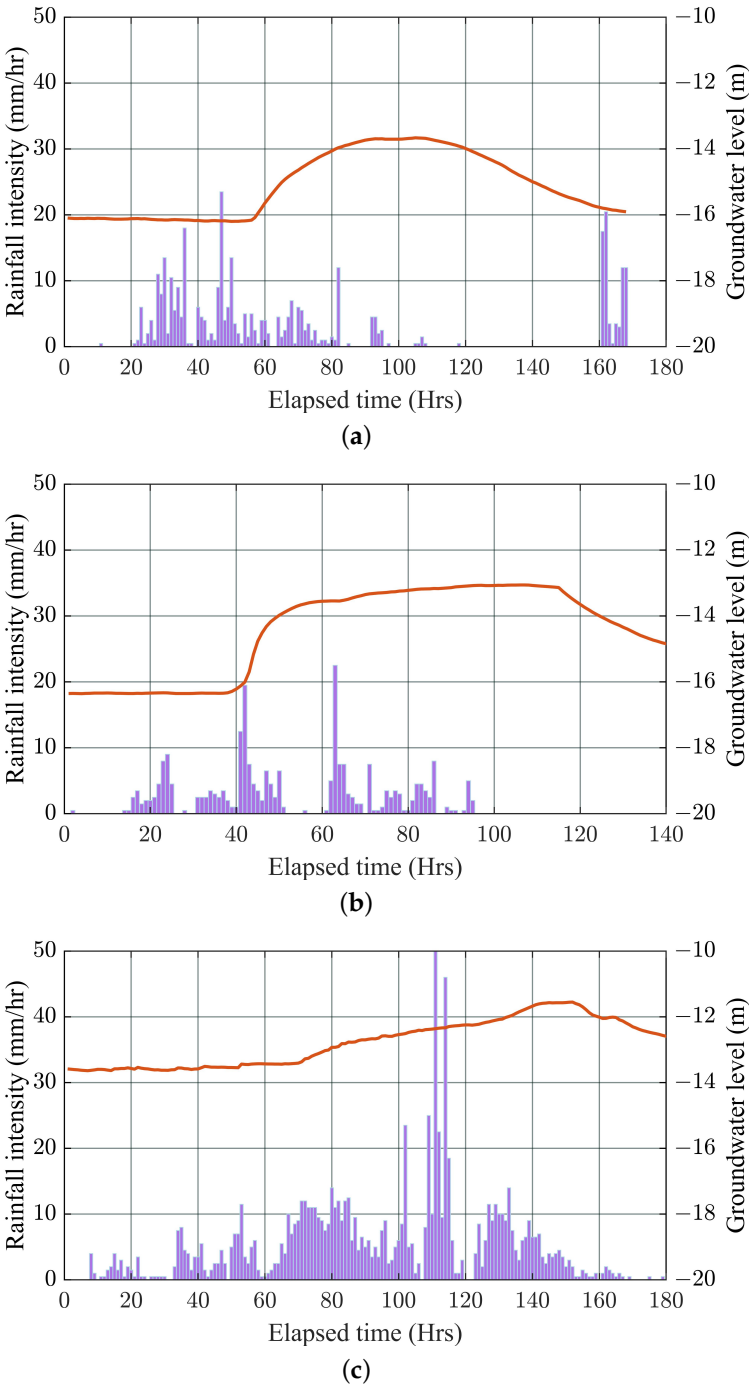


Figure 6. Rainfall intensity and groundwater level recorded during (**a**) Typhoon Kompasu (10∼16 October 2021), (**b**) May 24 heavy Plum Rain (24∼29 May 2022), and (**c**) Typhoon Nesat (10∼19 October 2022).

Figure 7 shows the horizontal displacement profiles recorded by the dual-function inclinometer/observation well (S04) and a standard inclinometer well (S05) between 12 November 2021 and 19 October 2022. The initially smooth, zig-zag horizontal displacement profiles in Figure 7a,b reveal that the first 24 m of the ground could be subjected to compression by downward negative friction of the weathered SS/SH inter-layer [30]. On 19 October 2022, the profile went haywire, and eventually, the dual-function inclinometer/observation well was found to be damaged and had to be replaced by a standard inclinometer (S04*) (Figure 1). Figure 7c shows a sudden increase in the horizontal displacement to a value slightly less than 150 mm on 19 October 2022 during Typhoon Nesat, and

Figure 7c,d indicate the existence of a shear zone at depths between 13 and 15 m [30,31]. The lateral movements recorded by inclinometers S04 and S05 raise concerns regarding the stability of the study slope.

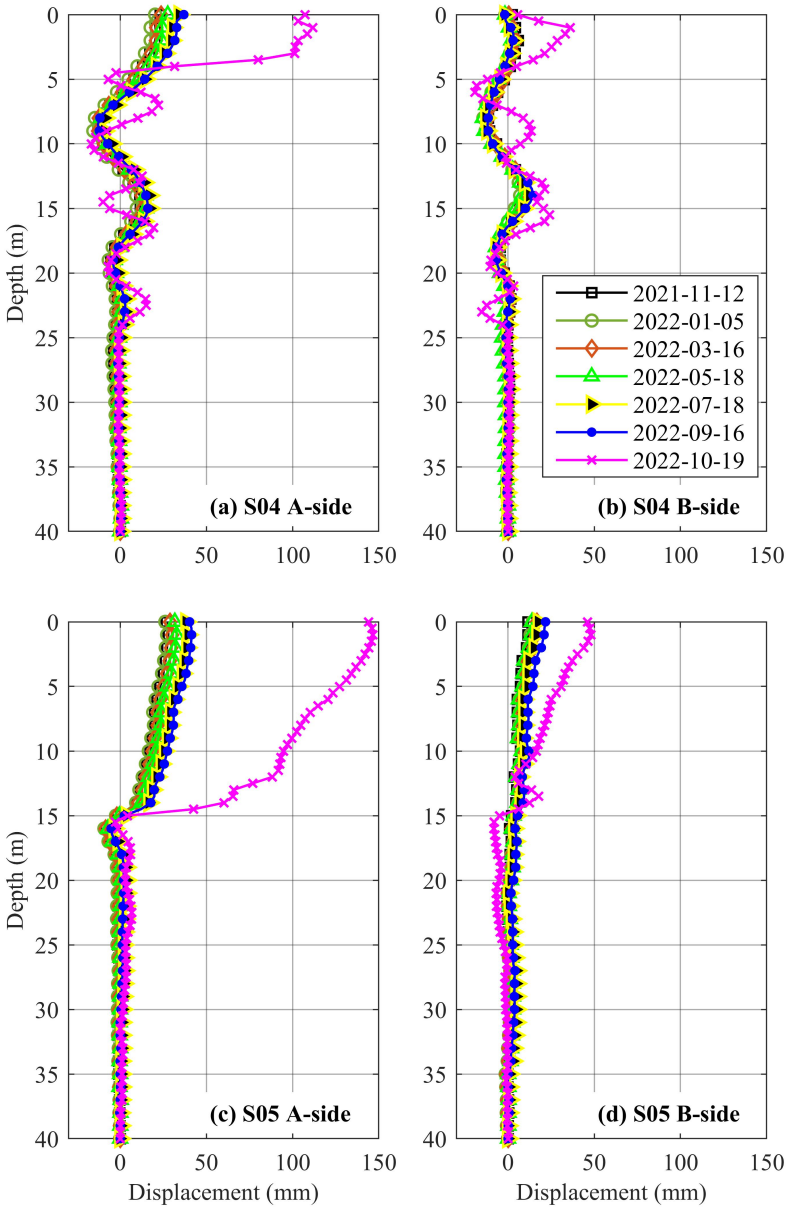


Figure 7. Horizontal displacement profiles measured by inclinometers: (**a**) S04 A side; (**b**) S04 B side; (**c**) S05 A side; (**d**) S05 B side.

3. Materials and Methods

Using a physically based method, we derived the rainfall threshold of the study slope through a series of finite-element analyses. The numerical model was built by considering the slope's geological features, and appropriate model elements and meshes were applied. The numerical model was validated by simulating the rise of groundwater levels due to the three heavy rainfalls; the numerical and site-recorded results were compared, and the results show a close agreement. We can conclude that the condition of the study slope was accurately simulated.

Once the finite-element model was successfully calibrated, transient infiltration analysis was implemented under the influence of the four rainfall distribution patterns to obtain the pore–water pressure distribution in the slope for use in the subsequent stability analysis. The stability results were interpreted to highlight critical failure mechanisms and derive the corresponding rainfall thresholds.

3.1. Formulation of Numerical Analysis

The Midas simulation program [32] uses equilibrium equations to ensure that a system remains in static equilibrium under applied loads by requiring the sum of forces and moments acting on the system to be zero. The equation for linear static analysis is expressed as follows:

$$[K]\{U\} = \{P\} \tag{1}$$

where $[K]$ is the stiffness matrix and $\{U\}$ and $\{P\}$ are the displacement and load vector, respectively.

The linear moment equilibrium equation for a small volume of a porous medium is expressed as follows [32]:

$$\nabla \cdot \boldsymbol{\sigma} + \rho \boldsymbol{g} = 0 \tag{2}$$

where ρ is the density of the porous medium; $\boldsymbol{g}$ is gravity acceleration; and $\boldsymbol{\sigma}$ is the total stress of the porous medium, defined based on an extension of Bishop's [33] stress relationship that considers partially saturated states for Terzaghi's [34] effective stress principle:

$$\boldsymbol{\sigma} = \boldsymbol{\sigma}' - \boldsymbol{m}[\chi u_w + (1 - \chi)u_a] \tag{3}$$

where $\boldsymbol{\sigma}'$ is the effective stress; $\boldsymbol{m}$ is the second-rank unit tensor; u_w and u_a are the pore–water and pore–air pressure, respectively; and χ is the effective stress parameter. According to Manenti et al. [35], who investigated a landslide on the slope of a water basin using a mixture model that accounts for the effects of soil saturation, the influence of landslide material saturation must be accounted for when simulating landslide dynamics because the motion of the saturated layer is more susceptible to higher deformation due to pore–water pressure that lowers the effective stresses in the solid matrix.

Richards' [36] equation represents the flow of water through unsaturated soils:

$$[C_e + S_e S]\frac{\partial H}{\partial t} + \nabla \cdot [-k\nabla(H + z)] = 0 \tag{4}$$

where H is the pressure head; z is the elevation head; S_e is the effective saturation; S is the storage coefficient; k is hydraulic conductivity; and C_e is the specific moisture capacity, which is related to the volumetric water content (θ) as follows:

$$C_e = \frac{\partial \theta}{\partial H} \tag{5}$$

The storage coefficient (S), which quantifies how much water can be stored or released from a unit volume of soil due to changes in the hydraulic head, is expressed as follows:

$$S = \frac{\Delta V}{V_0 \Delta h} \tag{6}$$

where ΔV is the change in the volume of stored water and Δh is the change in the hydraulic head.

To model soil behavior, particularly under large deformations, Midas uses constitutive models that can represent both elastic and plastic responses of soils, i.e., the Mohr–Coulomb failure criterion, which is commonly employed to define the yield surface:

$$\tau = c' + \sigma' \tan \phi \tag{7}$$

Thus, a combination of equilibrium equations, the Richards equation, the mass conservation principle, and the constitutive model for soil behavior is used to analyze this study's problem effectively.

3.2. Material Parameters

The soil–water characteristic curve (SWCC) is the most important input parameter in a typical rainfall infiltration analysis. The SWCC is usually represented by van Genuchten's [37] empirical formulation:

$$\theta_w = \theta_r + (\theta_s - \theta_r) \left[\frac{1}{[1 + (a\psi)^n]^{1-2/n}} \right] \tag{8}$$

where θ_w, θ_r, and θ_s are the volumetric, residual, and saturated water contents, respectively; ψ is the soil matric suction; and a and n are two fitting parameters. The fitting parameters for the study slope were a = 0.4369, n = 1.14, θ_r = 0.025, and θ_s = 0.5166.

The analysis adopted the hydraulic conductivity function proposed by van Genuchten [37]:

$$k = k_s \left[\frac{\left[1 - (a\psi)^{n-1} [1 + (a\psi)^n]^{-m} \right]^2}{[1 + (a\psi)^n]^m / 2} \right] \tag{9}$$

where k_s is the hydraulic conductivity of saturated soil; m is taken to be $1 - 1/n$, with referenced to Mualem [38]; and the two fitting parameters (a and n) are essentially the same parameters used in the corresponding SWCC. The interconnection and reliability of van Genuchten's SWCC and hydraulic conductivity functions were previously validated for silty soil by Gui and Hsu [39]. Table 2 shows the value of the saturated hydraulic conductivity (k_s) used in the study.

The numerical mesh used for the infiltration analysis is depicted in Figure 8. The numerical model also included existing retaining walls and a row of retaining piles to mimic the actual conditions at the site. Two-dimensional, triangular 3-node elements form the numerical mesh, which is often used in geotechnical finite-element analyses to better adapt to complex geometries, especially around irregular boundaries like slope faces, pile groups, and retaining structures. The mesh is refined near the retaining walls, retaining piles, and the slope crest area, and especially near the inclinometer (S04) and observation well (W01), where high-stress gradients and localized deformation are expected. The mesh becomes progressively coarser in the deeper and more distant zones to help optimize computational efficiency without compromising accuracy. In the mesh, both the left and right boundaries are designated as permeable, while the bottom boundary is impermeable. Additionally, the ground surface is configured as a rainfall infiltration boundary. The rainfall intensity used for the analysis is shown in Figure 6. For solid mechanics analysis, the movement of the left and right boundaries is restrained horizontally. In contrast, the bottom boundary is restrained from both horizontal and vertical movements. The soil parameters used in this study are shown in Table 2.

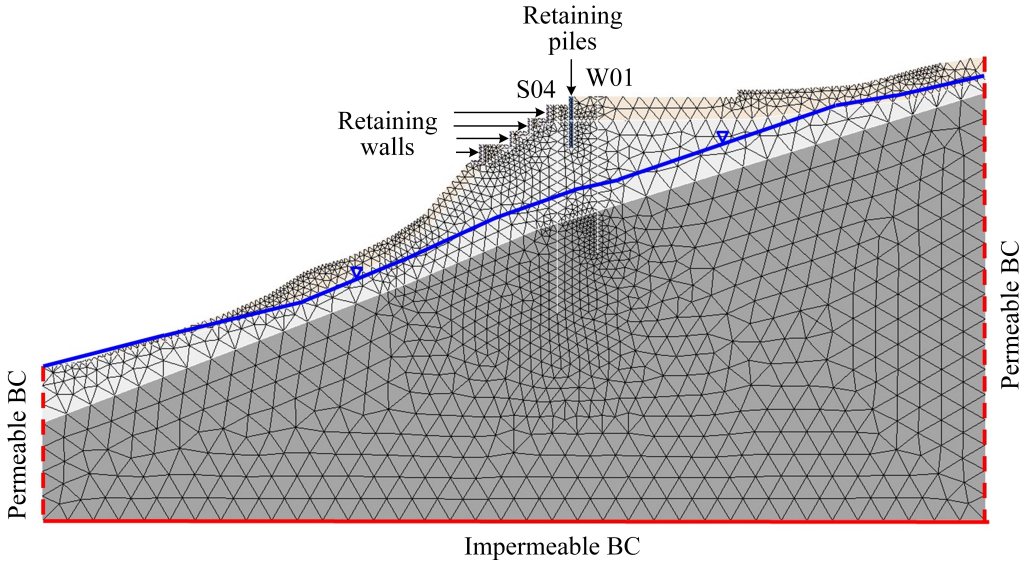


Figure 8. Typical mesh used in the numerical analysis.

Table 2. Material properties used in the numerical analysis.

Materials Property	Fill (F)	Weathered SS/SH	SS/SH
Bulk unit weight (kN/m^3)	19.62	23.54	23.54
Saturated unit weight (kN/m^3)	20.62	24.54	24.54
Poisson's ratio of soil	0.35	0.35	0.30
Apparent cohesion, c' (kPa)	0	8.0	49.0
Angle of internal friction, ϕ' (^{o})	26	28.4	29.4
Young's modulus of soil (MPa)	10	40	80
Saturated hydraulic conductivity, k_s (m/s)	2.75×10^{-4}	8.3×10^{-5}	8.0×10^{-8}
SWCC Parameter a	2	10.6	10.6
SWCC Parameter n	1.41	1.37	1.37
Saturated water content, θ_s	0.45	0.46	0.46
Residual water content, θ_r	0.067	0.034	0.034

4. Results

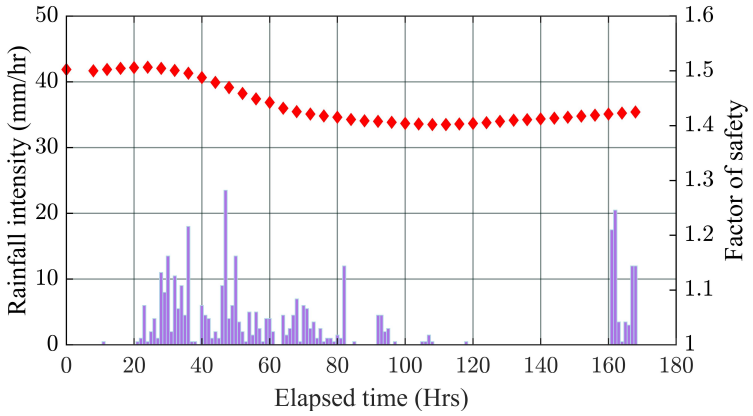
4.1. Calibration of Numerical Model

We verified the numerical model and soil hydraulic parameters via the simulation of rainfall infiltration during the three heavy rainfall events (Figure 6), i.e., (i) Typhoon Kompasu (10∼16 October 2021), (ii) the May 24 Plum Rain (24∼29 May 2022), and (iii) Typhoon Nesat (10∼19 October 2022). Table 3 compares the site-recorded and numerically calculated peak groundwater levels during the three rainfall events. The results show that the maximum variation between the numerical and site-recorded valued is 6.67%. The Root Mean Square Error ($RMSE$), which quantifies the absolute error in the predictions of the observed and analyzed peak groundwater levels, is 0.54, indicating accurate predictions. The coefficient of determination (R^2), which indicates the degree to which the analyzed data fit the observed data, is 0.9962, showing that the analyzed data fit the observed data well. Although obtained with limited data points, the $RMSE$ and R^2 results suggested that the adopted numerical model and hydraulic parameters used to simulate groundwater levels under varying rainfall conditions are reliable.

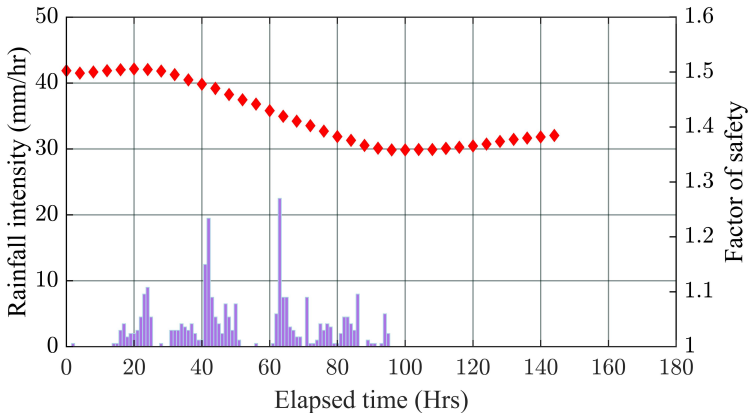
The subsequent stability analysis required the input of the pore–water distribution generated from the infiltration analyses. Figure 9 presents the factor-of-safety results from the stability analyses for Typhoon Kompasu, the May 24 Plum Rain, and Typhoon Nesat.

Table 3. Comparison between the observed and analyzed peak groundwater levels during the three heavy rainfall events.

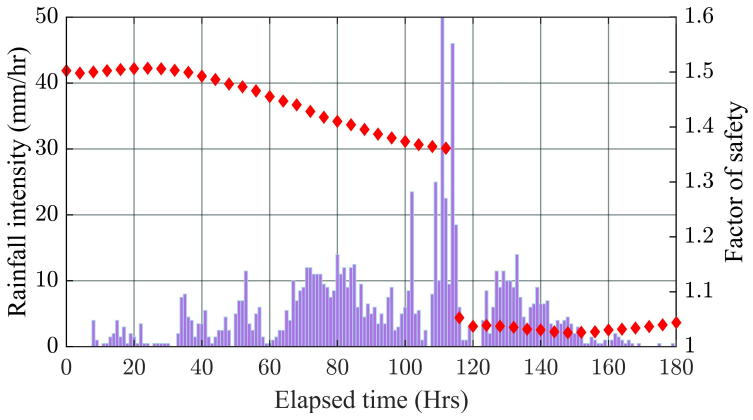
Rain Event	Observation Well No.	Observed (m)	Analyzed (m)	Variation (%)
Typhoon Kompasu	S04	−13.66	−14.03	2.71
May 24 Plum rain	S04	−13.10	−13.48	2.90
Typhoon Nesat	W01	−11.55	−12.32	6.67



(**a**)



(**b**)



(**c**)

Figure 9. Rainfall intensity and simulated factor of safety during (**a**) Typhoon Kompasu (10∼16 October 2021), (**b**) the May 24 Plum Rain (24∼29 May 2022), and (**c**) Typhoon Nesat (10∼19 October 2022).

The factor of safety at $t = 0$ prior to the landing of Typhoon Kompasu was about 1.50, as shown in Figure 9a, and the rain brought by Typhoon Kompasu started to fall at $t = 20$ h. However, the safety factor remained unchanged until 12 h later, when it decreased to a minimum value of 1.39 at the 108th hour. The factor of safety for the May 24 Plum Rain is plotted in Figure 9b; the analysis result shows that the factor of safety decreased to 1.35 at the 96th hour. These results show that the slope was stable during Typhoon Kompasu and the May 24 Plum Rain. With respect to Typhoon Nesat, Figure 9c shows that there is a sharp decrease in the factor of safety at the 116th hour. It reaches the minimum value of 1.02 at the 148th hour, indicating the slope is critical.

4.2. Alert and Action Values

An alert value is a specific rainfall threshold that, when reached, triggers a warning or alert to indicate the possibility of a hazard; the value serves to notify relevant authorities and the public about potential risks associated with heavy rainfall. An action value refers to when a specific rainfall threshold is reached, requiring the execution of pre-specified responses, such as evacuation or other emergency actions. In other words, the alert value informs potential hazards, while the action value initiates emergency responses.

Before determining the alert and action values, this study first defined four types of cumulative rainfall: $R1$, $R2$, $R3$, and $R4$, where

1. $R1$ is the cumulative rainfall when the factor of safety (FOS) is one;
2. $R2$ is the cumulative rainfall recorded three hours before $FOS = 1$ is reached;
3. $R3$ is the cumulative rainfall recorded five hours before $FOS = 1$ is reached;
4. $R4$ is the cumulative rainfall when the FOS is 1.1.

The alert value is taken to be the minimum of $\{R1, R2, R3,$ and $R4\}$, while $R2$ is defined as the action value, which is the cumulative rainfall recorded three hours before the slope acquired an FOS of one; three hours are deemed sufficient to implement emergency response in Taipei City.

Based on the numerical model and the four rainfall distribution patterns (uniform, intermediate, advanced, and delayed, as shown in Figure 4), the studied slope was analyzed under the four rainfall distribution patterns with rainfall durations of 24 and 72 h to determine the corresponding 24 and 72 h cumulative rainfall thresholds. The total cumulative rainfall values for the 24 and 72 h distributions are 720 mm and 2160 mm, respectively.

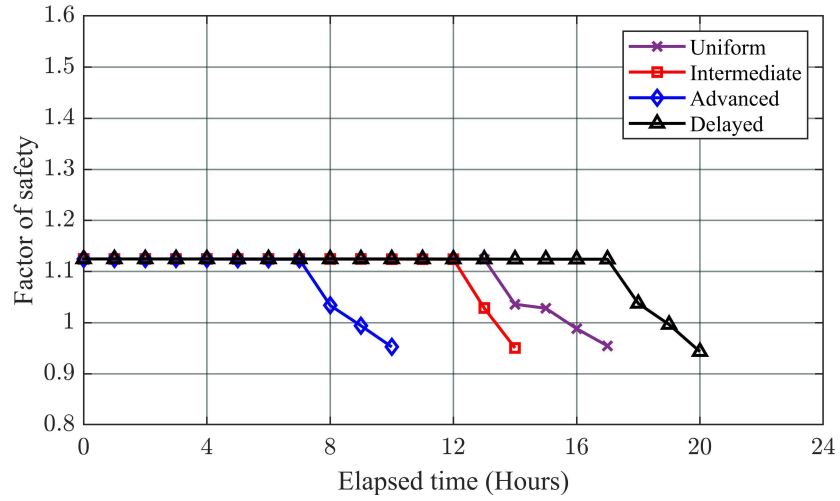
4.2.1. Short Duration: 24 h Rainfall

Figure 10a,b show the slope's factor of safety versus elapsed time and cumulative rainfall, respectively. Figure 10a and Table 4 reveal that the slope under the advanced rainfall pattern failed ($FOS = 1$) at 8.8 h after the rain started; under the intermediate rainfall pattern, the slope failed at 13.9 h, while under the uniform patterns, the slope failure time was 15.70 h. As expected, under the delay pattern, the slope failed, at the latest, at 18.9 h, towards the end of the rainfall duration. Under advanced rainfall patterns, rainwater infiltrates quicker into the soil than under the other rainfall patterns, leading to immediate saturation and weakening of the shear strength, which explains why landslides occur faster under this condition.

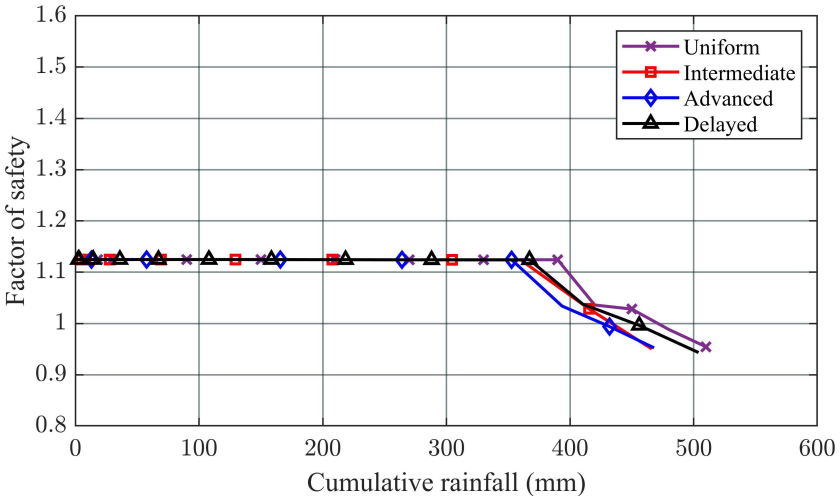
The values of $R1$, $R2$, $R3$, and $R4$ for all four rainfall patterns, as derived from Figure 10b, are summarized in Table 5 for comparison. Among these cumulative values, $R1$, the rainfall corresponding to $FOS = 1$, i.e., when failure is defined, is the largest among. The alert value for each of the four distribution patterns is the minimum of $\{R1, R2, R3,$ and $R4\}$; the minimum value of 207.7 mm is the 24 h alert value of the studied slope. The action value for each of the four distribution patterns is $R2$, the cumulative rainfall recorded three hours before reaching $FOS = 1$; the minimum of these $R2$ values, 304.6 mm, is the 24 h action value of the studied

slope. The alert and action cumulative rainfalls are almost identical, with the advanced pattern slightly higher than that of the intermediate pattern; however, the slope under the advanced pattern failed five hours earlier than the slope under the intermediate pattern. A yellow alert is triggered when 200 mm or more of rain is expected within 24 h as a practical approximation of the 207.7 mm threshold, while a red alert is triggered when 300 mm or more of rain is expected within 24 h as a practical approximation of the 304.6 mm threshold.

The yellow alert threshold is set slightly below the calculated minimum alert value of 207.7 mm to identify potential risks early to allow for a buffer against potential underestimation of rainfall and to provide time for preventive measures. It also aligns in the simplification of communication and decision making by using a round number. The yellow alert threshold may result in false alarms, but the benefits of detecting an early warning outweigh the potential drawbacks. In contrast, the 300 mm red alert threshold represents a higher risk level and requires immediate action. The choice of 300 mm should be dynamically reviewed to ensure it can capture the most critical scenarios without causing unnecessary panic.



(**a**)



(**b**)

Figure 10. Relationship between factor of safety and (**a**) elapsed time and (**b**) cumulative rainfall, under a 24-h rainfall.

Table 4. The time at which $FOS = 1.12$ started to fall and reach its critical value under various 24-h rainfall patterns (see Figure 10a).

Rainfall Pattern	Time When $FOS = 1.12$ Begins to Fall	Time When $FOS = 1$	$t_{cr} - t_1$
	t_1 (Hours)	t_{cr} (Hours)	Δt (Hours)
Advanced	7.27	8.80	1.53
Intermediate	12.25	13.90	1.65
Delayed	17.28	18.90	1.61
Uniform	13.70	15.70	2.00

Table 5. Determination of the alert and action values for 24 h rainfall.

Rainfall Pattern \ Cumulative Rainfall	*R*1	*R*2	*R*3	*R*4	Alert Value	Action Value
Advanced pattern (mm)	426.2	309.6	216.0	363.7	216.0	309.6
Intermediate pattern (mm)	433.9	304.6	207.7	374.0	207.7	304.6
Delayed pattern (mm)	451.9	326.4	252.0	379.3	249.0	323.0
Uniform pattern (mm)	471.1	390.0	330.0	398.3	321.1	381.1

Note(s): *R*1 is the cumulative rainfall when the *FOS* is one, *R*2 is the cumulative rainfall recorded 3 h before an *FOS* of 1 is reached, *R*3 is the cumulative rainfall recorded 5 h before an *FOS* of 1 is reached, and *R*4 is the cumulative rainfall when the *FOS* is 1.1. The numerical value in the boxes denotes the minimum value of the alert and action value, respectively.

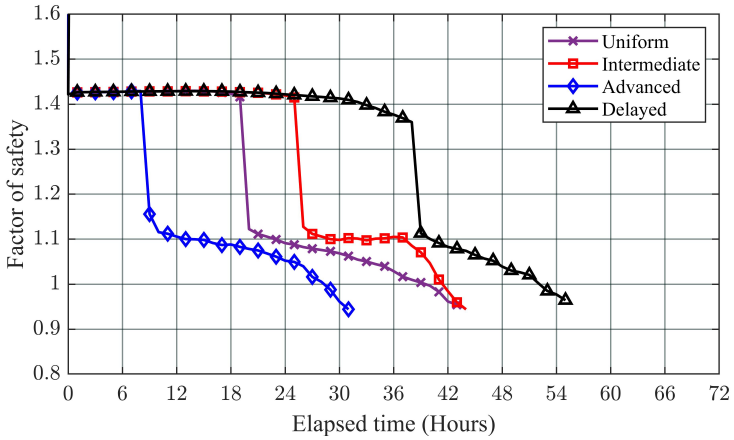
4.2.2. Long Duration: 72-h Rainfall

Figure 11a shows the relationship between the factor of safety and elapsed time for four different 72 h rainfall distribution patterns. At $t = 0$ h, all patterns start with a factor of safety of about 1.42, indicating a stable condition. As rain starts, the slope remains stable until a specific time, depending on the distribution patterns, when it suddenly weakens and the corresponding factor of safety drops drastically to 1.1. However, the slope is still stable. The time at which the slope suddenly weakens and the time when its $FOS = 1$ for all rainfall patterns are summarized in Table 6.

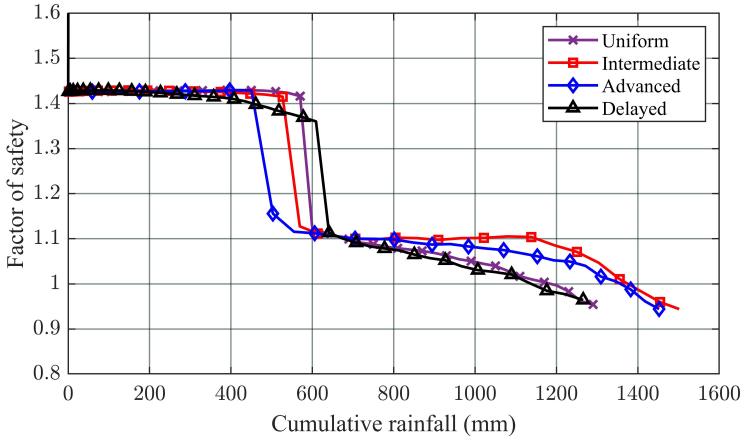
Table 6. The time at which the *FOS* started to fall sharply and reach its critical value under various 72-h rainfall patterns (see Figure 11a).

Rainfall Pattern	Time *FOS* Falls From		Time *FOS* Fall To		Time When $FOS \leq 1$
	FOS_1	t_1	FOS_2	t_2	t_{crit}
Advanced	1.42	8	1.16	9	28.3
Intermediate	1.42	25	1.13	26	41.4
Delayed	1.36	38	1.11	39	52.1
Uniform	1.42	19	1.12	20	39.5

Table 6 shows that the advanced pattern is the most concerning, as the initially stabilized slope weakened drastically eight hours after the rain started. However, it took another 20.3 h before destabilization, while the delayed pattern remained safe for 38 h before weakening sharply and took another 14.1 h before destabilizing. The differences between the time when weakening started and destabilization highlight how different rainfall distribution patterns influence the stability of the slope over time. The advanced pattern initialized failure at $\frac{1}{9}$ of the rainfall duration, while the delayed pattern initialized failure at $\frac{19}{36}$ of the rainfall duration. The advanced pattern reveals immediate risks and requires immediate action as soon as rainfall starts.



(**a**)



(**b**)

Figure 11. Relationship between factor of safety and (**a**) elapsed time and (**b**) cumulative rainfall under a 72-h rainfall.

The values of various cumulative rainfalls ($R1$, $R2$, $R3$, and $R4$) for all four rainfall patterns, as derived from Figure 11b, are summarized in Table 7 for comparison. Similar to the procedures shown in Section 4.2.1, the 72-h rainfall's action and alert values for the studied slope are 494.5 mm and 1012.0 mm, respectively.

Table 7. Determination of the alert and action values for 72-h rainfall.

Rainfall Pattern \ Accumulated Rainfall	*R*1	*R*2	*R*3	*R*4	Alert Value	Action Value
Advanced (mm)	1357.3	1244.6	1165.4	494.5	494.5	1244.6
Intermediate (mm)	1375.7	1217.1	1103.2	558.6	558.6	1217.1
Delayed (mm)	1138.1	1012.0	932.1	629.8	629.8	1012.0
Uniform (mm)	1185.9	1095.9	1035.9	592.1	592.1	1095.9

Note(s): $R1$ is the cumulative rainfall when the *FOS* is one, $R2$ is the cumulative rainfall recorded 3 h before an *FOS* of one is reached, $R3$ is the cumulative rainfall recorded 5 h before an *FOS* of one is reached, and $R4$ is the cumulative rainfall when the *FOS* is 1.2. The numerical value in the boxes denotes the minimum value of the alert and action value, respectively.

One significant difference observed in the analysis between the 24 and 72 h long rainstorms is the type of failure the slope acquired. In general, shallow failure is observed

in the 24-h rainfall while deeper failure is observed in the 72 h rainfall (Figure 12). Intense rain mainly triggers shallow landslides over a short period (one day). However, for a prolonged rain that continues for a few days, the water infiltrates deeper into the ground and causes deeper and more devastating failures.

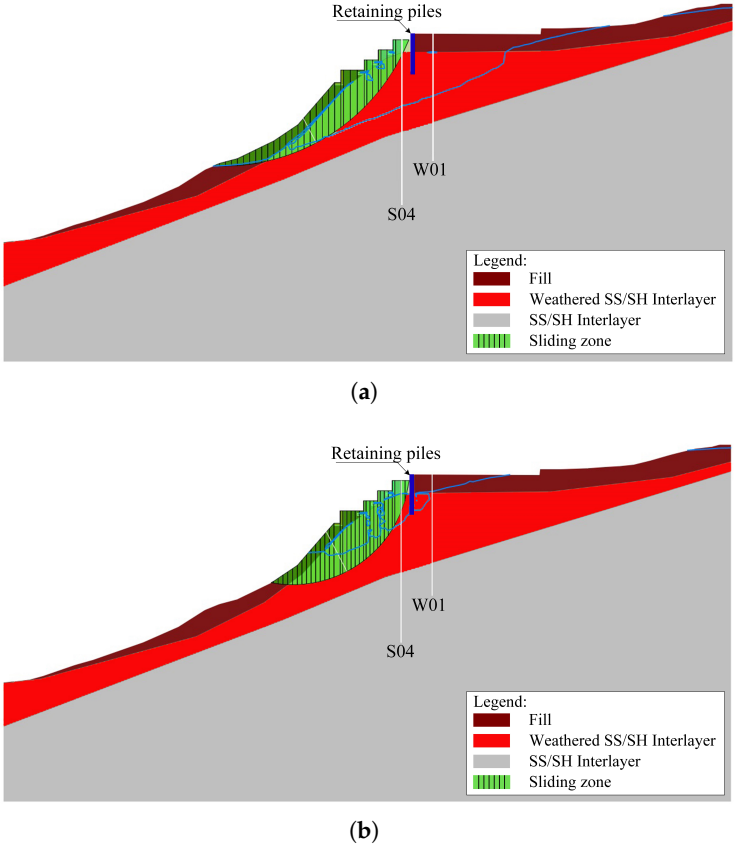


Figure 12. Types of generated failure: (**a**) shallow failure (24 h rain); (**b**) deep failure (72 h rain).

5. Discussion

Figure 13 shows the historical daily rainfall between 1 January 2008 and 31 December 2024; the daily rainfalls that exceeded 200 mm and 300 mm correspond to the alert and action threshold, respectively. A total of 24 rainfall events recorded a daily rainfall exceeding 200 mm/24 h, i.e., reaching the alert level, of which 12 had daily rainfall exceeding 300 mm/24 h, i.e., reaching the action level. The 12 events were Typhoons Sinlaku, Jangmi, and Morakot (2009), Typhoons Fanapi and Megi (2010), the 10 June 2012 Plum Rain, and Typhoon Saola (2012; retaining-wall displacement on the lower slope of the western platform of the study slope); Typhoons Soudelor and Dujuan (2015; retaining-wall displacement on the lower slope of the western platform), Typhoon Megi (2016; cracking on the western platform), Typhoon Nesat (2022; cracking on the western platform and slope displacement on the lower slope), and Typhoon Kongrey (2024).

Previously, alert and action warnings were based on higher rainfall amounts. However, Typhoon Nesat in October 2022 showed that instability risks could happen with less rain than expected and prompted engineers to lower the previous rainfall alert thresholds: from 400 mm/24 h to 200 mm/24 h for the alert threshold and from 500 mm/24 h to 300 mm/24 h for the action threshold, as recommended. Based on the new alert ($\geq$200 mm/h) and action ($\geq$300 mm/h) thresholds, on average, over 17 years, Taipei City would issue 1.41 yellow alerts and 0.70 red alerts (calling for evacuation protocols) per annum. After implementing the new alert and action thresholds, in July 2024, during Typhoon Kaemi, a cumulative

rainfall of 206.5 mm/h triggered a yellow alert and, subsequently, a red alert (302 mm/h), both of which were lifted after rainfall subsided. Two months later, heavy rains in late September 2024 repeatedly activated yellow alerts (200–200.5 mm/24 h), which were deactivated once the rainfall subsided below the threshold value. On 31 October 2024, Typhoon Kongrey escalated from a yellow alert (200.5 mm/h) to a red alert (302 mm/h), which was lifted on 1 November after the 6 h rainfall dropped to 4.5 mm. These incidents suggest the need for dynamic threshold adjustments to ensure timely evacuations and enhance slope safety management.

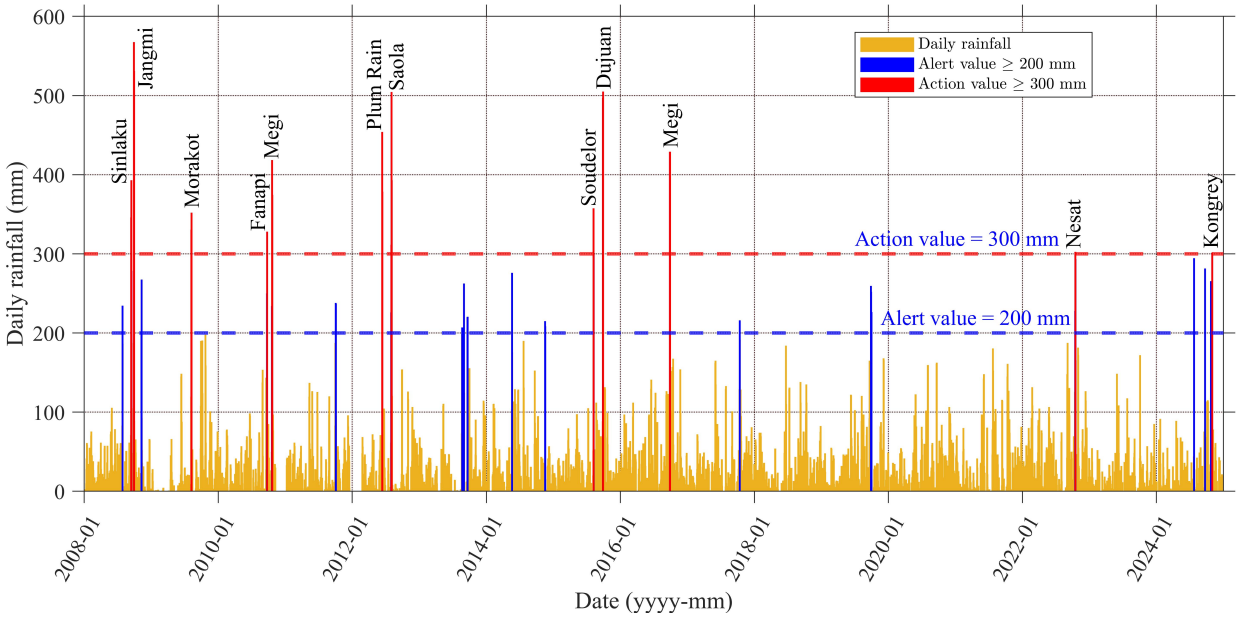


Figure 13. Historical daily rainfall and typhoons recorded between 1 August 2008 and 31 December 2024.

5.1. Impact of Rainfall Patterns on Slope Stability

The study revealed that different rainfall distribution patterns significantly influence the time of landslide initiation. The results presented in Figure 10 show that advanced rainfall patterns, where peak rainfall occurs early, lead to the most rapid slope failure (7.27 h). In contrast, delayed patterns resulted in the slowest slope destabilization due to a gradual increase in groundwater levels because of prolonged infiltration.

Another important finding from this study is that heavy rainfall over a short period ($\leq$24 h) tends to trigger shallow landslides. In contrast, more extended periods of rain ($\geq$72 h) are more likely to cause deep landslides. This result is consistent with previous studies, such as those conducted by Fathiyah and Erly [28] and Yang et al. [29], who found that prolonged rainfall patterns contribute to deep rather than shallow failure surfaces. This difference is vital for the development of early warning systems for landslides because it suggests that different strategies might be needed to prevent or respond to these failures.

5.2. Practical Applications for Landslide Mitigation

This study provides a scientific basis for integrating numerical modeling into real-world disaster preparedness strategies. The derived rainfall thresholds can be incorporated into the following areas:

1. Early warning systems, where automated rainfall sensors and slope monitoring units can use the established thresholds to trigger real-time alerts [40,41];
2. Urban planning and infrastructure resilience, in which authorities can revise regulations to restrict construction in high-risk zones where thresholds are frequently exceeded [42,43];

3. Disaster response protocols, where emergency response teams can use these data to pre-position resources, such as temporary shelters and evacuation routes, in landslide-prone areas [44,45].

5.3. Limitations of the Study

While this study provides valuable insights, future studies could address, for example, the increasing frequency and intensity of typhoons due to extreme climate change, which may render historical rainfall data less reliable for future predictions; therefore, dynamic climate models should be incorporated to adjust thresholds accordingly.

Although the numerical model was calibrated using past events, real-time field measurements, such as those collected by observation wells, soil moisture sensors, and inclinometers, should be used to validate and improve predictions under active storm conditions. Further studies could also explore machine learning integration to maintain data integrity [46] and enhance threshold prediction accuracy.

6. Conclusions

This study presented a physically based framework for defining rainfall thresholds to improve early landslide warning systems. The results of this study reveal the importance of integrating rainfall patterns, rainfall thresholds, and slope stability analysis into early landslide warning systems. We identified critical rainfall thresholds, which can serve as a basis for early landslide warning and risk assessment systems in Taipei City. The following findings and conclusions are reported:

1. This study shows that different rainfall patterns influence the timing and types of slope failure. Advanced rainfall patterns, where heavy rain occurs early, result in the most rapid slope destabilization, while delayed patterns lead to more gradual and deep failure due to prolonged infiltration.
2. This study shows that short-duration rainfall (24 h) mainly triggers shallow landslides, whereas prolonged rainfall (72 h) leads to deep landslides. This finding is crucial for early landslide warning systems, which provide different mitigation strategies based on the expected rainfall duration.
3. Before this study, yellow and red warnings were based on higher rainfall amounts, but recent storms showed that landslides can happen with less rain than expected. Based on the findings of this study, the Taipei City government revised the alert and action thresholds for issuing landslide warnings. This study suggests the importance of adjusting the thresholds dynamically, as evidenced by Typhoon Nesat (2022) and Typhoon Kongrey (2024), which triggered necessary evacuations. Implementing a dynamic rainfall threshold framework into the early warning systems for landslide-prone areas can improve rainfall-induced prevention strategies, protect lives, and mitigate landslide risks in urban and mountainous areas.
4. To enhance the accuracy and applicability of rainfall thresholds, future studies should incorporate real-time monitoring systems to improve numerical predictions, explore machine learning and AI techniques, and incorporate dynamic climate models to develop more dynamic and adaptive landslide prediction models.

Author Contributions: Conceptualization, H.-A.C., M.-C.C., L.-S.C. and M.-W.G.; analysis, H.-A.C., M.-C.C. and M.-W.G.; data curation, H.-A.C.; investigation, H.-A.C., M.-C.C., L.-S.C. and M.-W.G.; writing—original draft preparation, H.-A.C.; writing—review and editing, M.-C.C. and M.-W.G.; project administration, L.-S.C.; supervision, M.-C.C., L.-S.C. and M.-W.G. All authors have read and agreed to the published version of the manuscript.

Funding: A part of this study—the ground investigation, field monitoring, and numerical simulation—was based upon projects GEO-1105060, GEO-1115052, and GEO-1125042 supported by the Geotechnical Engineering Office, Public Works Department, Taipei City Government.

Data Availability Statement: The data presented in this study are included in the article.

Conflicts of Interest: Ming-Chien Chung were employed by the company Arbel Technical Consultants, Inc. The remaining authors declare that the research was conducted in the absence of any commercial or financial relationships that could be construed as a potential conflict of interest.

References

1. Typhoon Soudelor. Wikipedia, Wikimedia Foundation, 12 February 2025. Available online: https://en.wikipedia.org/wiki/Typhoon_Soudelor (accessed on 28 February 2025).
2. Mondini, A.C.; Guzzetti, F.; Melillo, M. Deep learning forecast of rainfall-induced shallow landslides. *Nat. Commun.* **2023**, *14*, 2466. [CrossRef] [PubMed]
3. Peng, B.; Wu, X.L. Optimizing rainfall-triggered landslide thresholds for daily landslide hazard warning in the Three Gorges Reservoir area. *Nat. Hazards Earth Syst. Sci.* **2024**, *24*, 3991–4013. [CrossRef]
4. Segoni, S.; Piciullo, L.; Gariano, S.L. A review of the recent literature on rainfall thresholds for landslide occurrence. *Landslides*x **2018**, *15*, 1483–1501. [CrossRef]
5. He, S.; Wang, J.; Liu, S. Rainfall Event–Duration Thresholds for Landslide Occurrences in China. *Water* **2020**, *12*, 494. [CrossRef]
6. Abraham, M.T.; Satyam, N.; Rosi, A.; Pradhan, B.; Segoni, S. The Selection of Rain Gauges and Rainfall Parameters in Estimating Intensity-Duration Thresholds for Landslide Occurrence: Case Study from Wayanad (India). *Water* **2020**, *12*, 1000. [CrossRef]
7. Abraham, M.T.; Satyam, N.; Kushal, S.; Rosi, A.; Pradhan, B.; Segoni, S. Rainfall Threshold Estimation and Landslide Forecasting for Kalimpong, India Using SIGMA Model. *Water* **2020**, *12*, 1195. [CrossRef]
8. Jordanova, G.; Gariano, S.L.; Melillo, M.; Peruccacci, S.; Brunetti, M.T.; Jemec Auflič, M. Determination of Empirical Rainfall Thresholds for Shallow Landslides in Slovenia Using an Automatic Tool. *Water* **2020**, *12*, 1449. [CrossRef]
9. Roccati, A.; Paliaga, G.; Luino, F.; Faccini, F.; Turconi, L. Rainfall Threshold for Shallow Landslides Initiation and Analysis of Long-Term Rainfall Trends in a Mediterranean Area. *Atmosphere* **2020**, *11*, 1367. [CrossRef]
10. Abraham, M.T.; Pothuraju, D.; Satyam, N. Rainfall Thresholds for Prediction of Landslides in Idukki, India: An Empirical Approach. *Water* **2019**, *11*, 2113. [CrossRef]
11. Dikshit, A.; Sarkar, R.; Pradhan, B.; Jena, R.; Drukpa, D.; Alamri, A.M. Temporal Probability Assessment and Its Use in Landslide Susceptibility Mapping for Eastern Bhutan. *Water* **2020**, *12*, 267. [CrossRef]
12. Deng, R.; Liu, H.; Zheng, X.; Zhang, Q.; Liu, W.; Chen, L. Towards Establishing Empirical Rainfall Thresholds for Shallow Landslides in Guangzhou, Guangdong Province, China. *Water* **2022**, *14*, 3914. [CrossRef]
13. Distefano, P.; Peres, D.J.; Piciullo, L.; Palazzolo, N.; Scandura, P.; Cancelliere, A. Hydro-meteorological landslide triggering thresholds based on artificial neural networks using observed precipitation and ERA5-Land soil moisture. *Landslides* **2023**, *20*, 2725–2739. [CrossRef]
14. Guo, B.; Pei, X.; Xu, M.; Li, T. Analyzing Rainfall Threshold for Shallow Landslides Using Physically Based Modeling in Rasuwa District, Nepal. *Water* **2022**, *14*, 4074. [CrossRef]
15. Bordoni, M.; Corradini, B.; Lucchelli, L.; Valentino, R.; Bittelli, M.; Vivaldi, V.; Meisina, C. Empirical and Physically Based Thresholds for the Occurrence of Shallow Landslides in a Prone Area of Northern Italian Apennines. *Water* **2019**, *11*, 2653. [CrossRef]
16. Ligong, S.; Sidek, L.M.; Hayder, G.; Mohd Dom, N. Application of Rainfall Threshold for Sediment-Related Disasters in Malaysia: Status, Issues and Challenges. *Water* **2022**, *14*, 3212. [CrossRef]
17. Gonzalez, F.C.G.; Cavacanti, M.D.C.R.; Ribeiro, W.N.; de Mendonça, M.B.; Haddad, A.N. A systematic review on rainfall thresholds for landslides occurrence. *Heliyon* **2023**, *10*, e23247. [CrossRef]
18. Cui, H.Z.; Tong, B.; Wang, T.; Dou, J.; Ji, J. A hybrid data-driven approach for rainfall-induced landslide susceptibility mapping: Physically-based probabilistic model with convolutional neural network. *J. Rock Mech. Geotech. Eng.* 2024, *In Press*. . [CrossRef]
19. *GEO: How to Differentiate Between Landslide and Slope Failure*; Department of Information and Tourism, Taipei City Government: Taipei, Taiwan, 2022. Available online: https://shorturl.at/eyX3N (accessed on 12 February 2025).
20. Geotechnical Engineering Office. *Landslide Predictive Studies and Multi-Temporal Remote Sensing Surface Deformation Analysis for Taipei City*; Report No. GEO1125042; Department of Public Works; Taipei City Government: Taipei, Taiwan, 2023; 318p. (In Mandarin)
21. Google Earth Pro 7.3.6.10201. Nangang, Taiwan: N25°01′35.46″, E121°39′37.41″. Available online: http://www.google.com/earth/index.html (accessed on 12 February 2025).

22. Yu, P.S.; Yang, T.C.; Kuo, C.C. Evaluating Long-Term Trends in Annual and Seasonal Precipitation in Taiwan. *Water Resour. Manag.* **2006**, *20*, 1007–1023. [CrossRef]
23. Huang, Y.Y. Analysis of Different Spatial-Temporal Rainfall Patterns on Groundwater Recharge: A Case Study in Pingtung Plain. Master Dissertation, National Central University, Taoyuan, Taiwan, 2020; 108p. (In Mandarin)
24. Lee, M.H. A Rainfall-Based Debris-Flow Warning Analysis and Its Application. Ph.D. Dissertation, National Cheng Kung University, Tainan, Taiwan, 2006; 229p. (In Mandarin)
25. Wu, L.Z.; Xu, Q.; Zhu, J.D. Incorporating hydro-mechanical coupling in an analysis of the effects of rainfall patterns on unsaturated soil slope stability. *Arab J. Geosci.* **2017**, *10*, 386. [CrossRef]
26. Gu, X.; Wang, L.; Ou, Q.; Zhang, W.G. Efficient stochastic analysis of unsaturated slopes subjected to various rainfall intensities and patterns. *Geosci. Front.* **2023**, *14*, 101490. [CrossRef]
27. Gu, X.; Wang, L.; Ou, Q.; Zhang, W.G.; Sun, G.H. Reliability assessment of rainfall-induced slope stability using Chebyshev–Galerkin–KL expansion and Bayesian approach. *Can. Geotech. J.* **2023**, *60*, 1909–1922. [CrossRef]
28. Fathiyah, H.S.; Erly, B. Parametric study on the effect of rainfall pattern to slope stability. In *MATEC Web of Conferences*; EDP Sciences: Les Ulis, France, 2017. . [CrossRef]
29. Yang, Y.S.; Yeh, H.F.; Ke, C.C.; Chen, N.C.; Chang, K.C. Assessment of probability of failure on rainfall-induced shallow landslides at slope scale using a physical-based model and fuzzy point estimate method. *Front. Earth Sci.* **2022**, *10*, 957506. [CrossRef]
30. Jeng, C.J.; Yo, Y.Y.; Zhong, K.L. Interpretation of slope displacement obtained from inclinometers and simulation of calibration tests. *Nat. Hazards* **2017**, *87*, 623–657. [CrossRef]
31. Ganjalipour, K. Review of inclinometer errors and provide correction methods for bias shift error and depth position error of the probe. *Geotech. Geol. Eng.* **2021**, *39*, 4017–4034. [CrossRef]
32. Midas Information Technology. *MIDAS FEA NX Analysis Manual: Chapter 3 Elements*; Midas IT: Seoul, Republic of Korea, 2019; p. 112. Available online: https://www.midasoft.com/hubfs/03_AnalysisReference_Chapter-3Elements.pdf (accessed on 12 February 2025)
33. Bishop, A.W. The principle of effective stress. *Tek. Ukebldad* **1959**, *106*, 859–863.
34. Terzaghi, K. Die Berechnung der Durchlässigkeitsziffer des Tones aus Dem Verlauf der Hydrodynamischen Spannungserscheinnungen. In *Mathematish-naturwissenschaftliche, Klasse*; Akademie der Wissenschaften: Vienna, Austria, 1923; Volume 132, pp. 125–138.
35. Manenti, S.; Amicarelli, A.; Todeschini, S. WCSPH with limiting viscosity for modelling landslide hazard at the slopes of artificial reservoir. *Water* **2018**, *10*, 515. [CrossRef]
36. Richards, L.A. Capillary conduction of liquids through porous mediums. *Physics* **1931**, *1*, 318–333. [CrossRef]
37. van Genuchten, M.T. A closed-form equation for predicting the hydraulic conductivity of unsaturated soils. *J. Soil Science Soc. Am.* **1980**, *44*, 892–898. [CrossRef]
38. Mualem, Y. A new model for predicting the hydraulic conductivity of unsaturated porous media. *Water Resour. Res.* **1976**, *12*, 513–522. [CrossRef]
39. Gui, M.W.; Hsu, C.S. Generalized fitting parameters of three permeability functions for predicting water coefficient of permeability of Lateritic soil. *Geotech. Testing J. ASTM* **2009**, *32*, 418–427. [CrossRef]
40. Wu, Y.B.; Niu, R.Q.; Yi Wang, Y.; Chen, T. A Fast Deploying Monitoring and Real-Time Early Warning System for the Baige Landslide in Tibet, China. *Sensors* **2020**, *20*, 6619. [CrossRef] [PubMed]
41. Liu, K.; Wei, S. Real-time debris flow monitoring and automated warning system. *J. Mt. Sci.* **2024**, *21*, 4050–4061. [CrossRef]
42. Zhang, X.; Song, J.; Peng, J.; Wu, J. Landslides-oriented urban disaster resilience assessment—A case study in ShenZhen, China. *Sci. Total Environ.* **2019**, *661*, 95–106. [CrossRef] [PubMed]
43. Farinós-Dasí, J.; Pinazo-Dallenbach, P.; Peiró Sánchez-Manjavacas, E.; Rodríguez-Bernal, D.C. Disaster risk management, climate change adaptation and the role of spatial and urban planning: evidence from European case studies. *Nat. Hazards* **2024**, . [CrossRef]
44. Highland, L.M.; Bobrowsky, P. *The Landslide Handbook—A Guide to Understanding Landslides*; U.S. Geological Survey Circular 1325; U.S. Department of the Interior, U.S. Geological Survey: Reston, VA, USA, 2008; 129p. Available online: https://pubs.usgs.gov/circ/1325/ (accessed on 14 April 2025).
45. Tsai, Y.-J.; Syu, F.-T.; Shieh, C.-L.; Chung, C.-R.; Lin, S.-S.; Yin, H.-Y. Framework of Emergency Response System for Potential Large-Scale Landslide in Taiwan. *Water* **2021**, *13*, 712. [CrossRef]
46. Lee, S.; Kim, Y.; Ji, B.; Kim, Y. Addressing missing data in slope displacement monitoring: Comparative analysis of advanced imputation methods. *Buildings* **2025**, *15*, 236. [CrossRef]

Disclaimer/Publisher's Note: The statements, opinions and data contained in all publications are solely those of the individual author(s) and contributor(s) and not of MDPI and/or the editor(s). MDPI and/or the editor(s) disclaim responsibility for any injury to people or property resulting from any ideas, methods, instructions or products referred to in the content.